



*Citation for published version:*

Chiereghin, N, Bull, S, Cleaver, DJ & Gursul, I 2020, 'Three-dimensionality of leading-edge vortices on high aspect ratio plunging wings', *Physical Review Fluids*, vol. 5, no. 6.  
<https://doi.org/10.1103/PhysRevFluids.5.064701>

*DOI:*

[10.1103/PhysRevFluids.5.064701](https://doi.org/10.1103/PhysRevFluids.5.064701)

*Publication date:*

2020

*Document Version*

Publisher's PDF, also known as Version of record

[Link to publication](#)

©2020 American Physical Society

## University of Bath




### General rights

Copyright and moral rights for the publications made accessible in the public portal are retained by the authors and/or other copyright owners and it is a condition of accessing publications that users recognise and abide by the legal requirements associated with these rights.

### Take down policy

If you believe that this document breaches copyright please contact us providing details, and we will remove access to the work immediately and investigate your claim.

## Three-dimensionality of leading-edge vortices on high aspect ratio plunging wings

N. Chiereghin , S. Bull , D. J. Cleaver, and I. Gursul 

*Department of Mechanical Engineering, University of Bath, Bath BA2 7AY, United Kingdom*



(Received 8 November 2019; accepted 30 April 2020; published 1 June 2020)

To investigate the effect of sweep on the leading-edge vortex of high aspect ratio plunging wings, this article presents force, bending moment, and volumetric velocity measurements for high aspect ratio  $AR = 10$  wings with sweep angles of  $0^\circ$  and  $40^\circ$ . The effect of the sweep angle on the bending moment is the largest at the minimum effective angle of attack. This is because as the leading-edge vortex sheds it moves inboard on the unswept wing while moving outboard on the swept wing. Where the leg of the leading-edge vortex connects with the wing there is significant three-dimensional flow. The axial velocity along the vortex filament, which may be towards to the wing tip or the wing root (reversed flow), exhibits increasing magnitude as the effective angle of attack decreases and the vortex filament deforms. Reversed axial flow along the vortex filament has the largest magnitudes for the unswept wing. In the vortex core, jetlike, wakelike, and uniform axial velocity profiles were observed. Unlike the classical vortex breakdown, the transition from the jetlike to the wakelike axial flow does not appear to be abrupt. The measurements also revealed evidence of spanwise instabilities in the leading-edge vortex filament.

DOI: [10.1103/PhysRevFluids.5.064701](https://doi.org/10.1103/PhysRevFluids.5.064701)

### I. INTRODUCTION

Unsteady aerodynamics of airfoils play an important role in numerous applications, which include micro air vehicles [1], biologically inspired flows [2,3], helicopter blades [4], and aircraft wing loads due to unsteady wing motion, turbulence, and gusts [5]. In most of these applications, with increasing frequency and amplitude, flow separation near the leading edge becomes unavoidable and results in the formation of leading-edge vortices (also known as “dynamic stall” vortices for pitching wings). The leading-edge vortices over flapping wings of micro air vehicles and small, unmanned underwater vehicles may increase the unsteady forces on low aspect ratio wings, and hence may be beneficial for the performance and the control of small vehicles. Another engineering application where leading-edge vortices may develop is high aspect-ratio wings—over rotorcraft blades during dynamic stall, on wind turbine blades in the presence of in-flow turbulence, and on aircraft wings due to unsteady maneuver or gust-induced flow separation. In these cases, increased lift and pitching or bending moment may need to be alleviated.

Considerable progress has been made in understanding of dynamic stall vortices that develop over two-dimensional pitching airfoils [4,6,7]. Recent work also includes unsteady separation, formation and convection of leading-edge vortices (LEVs) on nominally two-dimensional airfoils with two-dimensional data sets [8,9], as well as two-dimensional modelling of vortex shedding [10–12]. For finite wings, the existence of tip vortices may be important, especially for low aspect ratio unsteady wings. As the tip vortex affects the flow separation and the roll-up of the vorticity near the leading edge, strong three-dimensionality is expected with decreasing aspect ratio of the wing. Previous experimental [13,14] and computational simulations [15–17] revealed how the leading-edge vortex (dynamic stall vortex) evolved into three-dimensional vortical structures. We note that

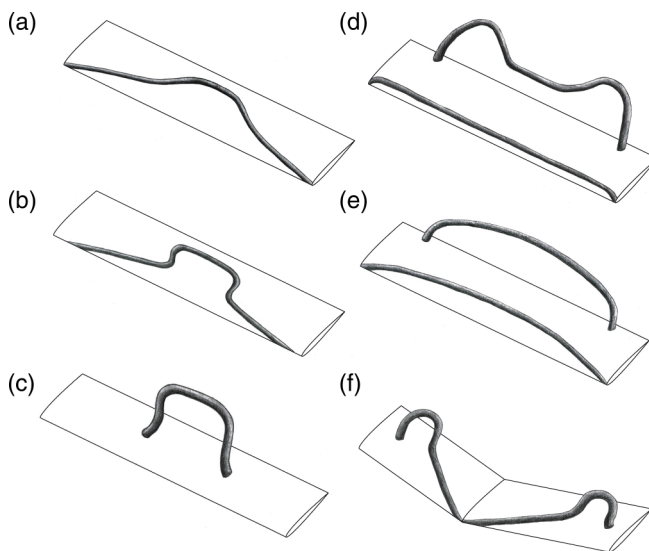


FIG. 1. Schematic of leading-edge vortices for aspect ratio  $AR = 4$  oscillating wings: (a),(b)  $\Omega$  vortex for pitching wings at  $k = 0.05$  [13,15,16]; (c) arch-type vortex at  $k = 0.20$  for a pitching wing [17]; (d) for a plunging wing at  $k = 1.88$  [19]; (e) for a plunging wing at  $k = 3.14$  [19]; (f) for a pitching swept wing [27].

the three-dimensional flows over rotating low aspect ratio wings [18] are not relevant to the present investigation as the physics of spanwise flow is different from nonrotating, but unsteady, wings. Figure 1 shows a schematic of leading-edge vortical structures at different reduced frequencies on pitching and plunging wings for an aspect ratio of  $AR = 4$ . In all cases, tip vortices and trailing-edge vortices are omitted for clarity. A degree of interpretation is used in the schematics taken from simulations and experiments. Computational simulations typically use the symmetry plane boundary conditions, effectively simulating a half model. Also, computational simulations contain small scale flow structures, which are omitted for clarity. Likewise, experimental simulations typically use half models, however velocity measurements are difficult to capture close to the viscous root plane. Nevertheless, it is generally true that the vortical structures remain approximately symmetric about the root plane.

It is likely that the most important parameters that govern the deformation of the vortex filament and three-dimensional shedding process are the wing aspect ratio and the reduced frequency. In Fig. 1 we focus on a single aspect ratio of  $AR = 4$  due to the abundance of measurements and simulations. Panels (a) and (b) were described as the development of a  $\Omega$  vortex for pitching wings at  $k = 0.05$  [13,15,16]. Here  $k = \pi fc/U_\infty$ , where  $f$  is the oscillation frequency,  $c$  is the chord length, and  $U_\infty$  is the freestream velocity. As the reduced frequency is increased to  $k = 0.20$  for a pitching wing in part (c), Visbal and Garmann [17] observed that the initial  $\Omega$  vortex develops into an arch-type vortex. As the leading-edge vortex spends relatively more time over the wing during the cycle with increasing reduced frequency, it may be considered to be under the influence of the tip vortices longer and this may facilitate the formation of the arch-type vortex. As discussed by Visbal and Garmann [17], the  $\Omega$ -shaped vortex is pinned at the wing-tip region and remains attached at the upstream corners. As it develops into an arch-type vortex, the legs move inboard and downstream, and are approximately normal to the wing surface. Eventually, the arch vortex develops into ringlike structures that are shed into the wake.

The arch-type vortices, with legs nearly perpendicular to the wing surface, are also observed over plunging wings [19–21]. Figure 1(d) illustrates the leading-edge vortex for a plunging wing at  $k = 1.88$  [19]. In this case and for higher reduced frequencies, we observe two leading-edge

vortices on the wing: one newly shed and the second one from the previous cycle. This is illustrated in Fig. 1(d). It appears that newly shed vortices are initially highly two-dimensional at these high reduced frequencies as a result of rapid roll-up of the vorticity into the concentrated leading-edge vortices. However, this long two-dimensional vortex filament exhibits significant deformation in the spanwise direction, which might also be facilitated by the dynamics of the tip vortex. Eventually a large arch-type vortex, with two legs near the outboard of the wing is observed as sketched in Fig. 1(d). At even a higher reduced frequency of  $k = 3.14$  for a plunging wing [19], Fig. 1(e) shows that the spanwise deformation is less than that of the lower reduced frequency case in panel (d), while the legs of the arch-type vortex is still near the outboard of the wing. The reason for the decreased deformation near the symmetry plane, which indicates a frequency sensitivity, is not known currently and deserves further investigation. Understanding the nature of the spanwise instabilities and three-dimensionality of the vortices is essential for developing flow control methods for wing-load alleviation and restriction of maximum unsteady lift and moment.

Overall, Fig. 1 displays the variety of vortical structures observed over low aspect ratio wings and suggests significant variations in the spanwise loading. However, a low aspect ratio wing may not be the most critical case in terms of root-bending moment. For high aspect ratio wings, due to the larger moment arm, the wing bending moment about the root may be more affected by the three-dimensionality of the flow separation and the dynamics of the leading-edge vortex (dynamic stall vortex) as the vortex interacts with the wing tip vortex. Recent surface pressure measurements revealed the three-dimensionality of the leading-edge vortex near the wing tip [22]. Numerical simulations also suggested that the wing tip region shows significant differences from inboard sections [23] and exhibits multiple dynamic stall cells over the span. We note that flow-field measurements are lacking in the literature for high aspect ratio wings. The first objective of this article is to investigate the effect of reduced frequency on the lift force and the root-bending moment for a high aspect ratio ( $AR = 10$ ) wing, and then focus on the dynamics of the separation and the leading-edge vortex development by means of volumetric velocity measurements, with particular attention to the region near the wing tip.

The second objective of this article is to understand the effect of leading-edge sweep for high aspect ratio wings. Chiereghin *et al.* [24] have investigated experimentally the impact of sweep angle ( $\Lambda = 0^\circ; 20^\circ; 40^\circ$ ) on the flow over a plunging wing ( $AR = 10$ ) at low Reynolds number of  $Re = 20\,000$ . The force, bending moment, and PIV measurements suggest that the leading-edge vortex dynamics becomes more influential on the forces and moments with increasing sweep angle. Recently, Gursul and Cleaver [25] have presented flow visualization that show that for a plunging ( $\Lambda = 40^\circ$  wing), a leading-edge vortex, similar to that found on delta wings, may form during certain phases of the unsteady wing motion. The dye flow visualization shown by Gursul and Cleaver [25] suggests that vortex breakdown occurs. The resulting region of highly three-dimensional flow covers a few chord lengths in the spanwise direction near the root. The development of the vortex near the junction is likely to depend on the airfoil shape and the leading-edge radius in addition to the reduced frequency. The dye flow visualization does not give a clear picture of the vortical flow after the breakdown, and the character of the dynamic stall vortex cannot be deduced. In a related investigation, Beem *et al.* [26] conducted experiments on high aspect ratio swept wings (with sweep angles up to  $45^\circ$ ), performing a transient plunging motion. Their PIV measurements were limited to the spanwise vorticity in two separate two-dimensional spanwise planes and flow visualization. The authors concluded that leading-edge vortex sheds and convects downstream for all sweep angles. The reduced frequency corresponded to  $k = 0.47$  and the maximum effective angle of attack reached  $35^\circ$ . This observation is in contrast with the observations reported by Gursul and Cleaver [25] for a sweep angle of  $40^\circ$ , at  $k = 1.41$  and maximum effective angle of attack of  $38^\circ$ , for which attached leading-edge vortices are possible.

For a smaller aspect ratio ( $AR = 4$ ) pitching swept wing, recent computational simulations [27,28] investigated the vortical flow structure in order to provide a model of three-dimensional dynamic stall vortex for  $\Lambda = 15^\circ$  and  $30^\circ$ . Our interpretation of their large-eddy simulations is given in Fig. 1(f). Two arch-type vortical structures develop over the full wing, unlike the unswept

wing cases. The vortex that develops from the apex region deforms into an arch-type vortex near the wing tip, where the outer leg of the arch vortex interacts with the wing-tip vortex. A recent article [29] investigated the three-dimensionality of the leading-edge vortex on a low aspect ratio wing ( $AR = 5$ ) with very low sweep angles ( $\Lambda = 11.3^\circ$  and  $16.7^\circ$ ). It was concluded that even though the magnitude of the spanwise flow inside the vortex is small, there was evidence of non-negligible vortex stretching and compression.

The vortex that develops from the leading-edge and the apex region deforms into an arch-type vortex near the wing tip, where the outer leg of the arch vortex interacts with the wing-tip vortex. These vortical structures will have a significant influence on the surface pressure and therefore forces and moments experienced by the wings. For applications such as fixed-wing aircraft with swept wings subjected to gusts or extreme maneuvers, this extra vortical contribution could create loads in excess of their design limits. Understanding the effect of sweep on the vortical flow is therefore necessary. To investigate the effect of sweep this article presents force, moment, and volumetric velocity measurements for high aspect ratio wings ( $AR = 10$ ) with wing sweep angles of  $\Lambda = 0^\circ$  and  $40^\circ$ .

## II. METHODOLOGY

Phase-averaged lift, bending moment, and volumetric three-component velocimetry measurements were conducted at  $Re = U_\infty c / \nu = 20\,000$  (where  $\nu$  is the kinematic viscosity) for three wings with (i) zero sweep angle with a NACA0012 cross section, (ii) sweep angle  $\Lambda = 40^\circ$  with a NACA0012 cross section, (iii)  $\Lambda = 40^\circ$  with a flat-plate cross section. The wings were subjected to a sinusoidal plunging motion  $h(t)$  normal to the freestream flow direction [Fig. 2(a)]:

$$h = a \cos(2\pi ft). \quad (1)$$

The effective angle of attack can be defined as the sum of the geometric angle of attack  $\alpha$  and the motion induced angle of attack due to the plunging motion:

$$\alpha_{\text{eff}}(t) = \alpha - \tan^{-1} \frac{1}{U_\infty} \frac{dh}{dt} = \alpha + \tan^{-1} \frac{V_{pl}}{U_\infty}. \quad (2)$$

A schematic representation of the wings and the coordinate system is shown in Fig. 2. All wings had the same chord length of  $c = 62.7$  mm. The angle of attack is set by rotating the wing around the  $z$  axis [Fig. 2(b)]. For the experiments described in this paper, the wing was set to a post-stall angle of attack of  $\alpha = 15^\circ$ . The reduced frequency of the plunging motion  $k$  ranged from 0.0 to 1.1 with a peak-to-peak amplitude of  $A/c = 0.5$ .

### A. Experiment

The experiments were conducted in the closed-loop free-surface water-tunnel facility at the University of Bath. The water tunnel has a glass working section with dimensions  $381 \times 508 \times 1530$  mm. The flow speed range is from 0 to 0.5 m/s with a turbulence intensity of less than 0.5% [30]. The wing is vertically mounted in the working section and linked to a translation stage generating a linear motion perpendicular to the freestream flow (see Fig. 3). Hence the plunging motion was applied at the wing root. The wings have an end-plate arrangement near the root, and therefore represent half models. This gives a semiaspect ratio of 5 and a full aspect ratio of  $AR = 10$ .

The wings with the NACA0012 profile were manufactured from PA 2200 polyamide using selective laser sintering with a polished smooth surface. In order to ensure a high spanwise stiffness, a T800 carbon fiber bar was inserted inside the wing with section  $25 \times 5$  mm. The wing deformation was monitored by the cameras used for measuring the velocity field. The maximum tip deformation did not exceed 1% of the model semispan. The flat-plate wing was manufactured from T800 carbon fiber with a thickness of 2.5 mm (4% $c$ ). The plate was machined with a bevel angle of  $45^\circ$  on the

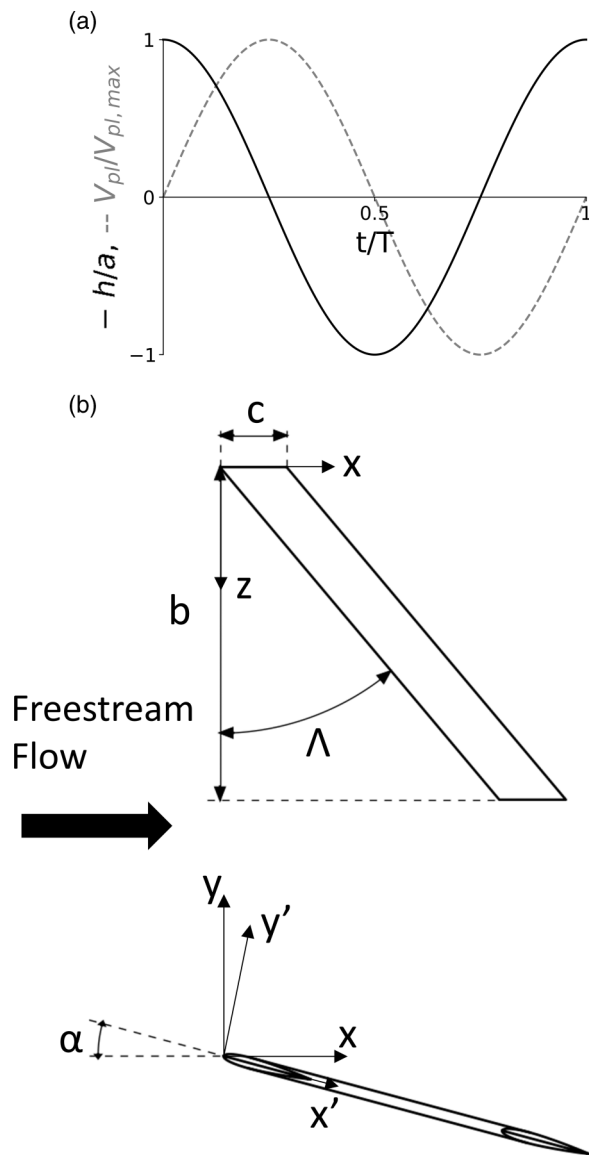


FIG. 2. (a) Plunging motion and plunge velocity; (b) top and side views of the wing and the coordinate system.

lower surface at the leading edge and trailing edge in order to create fixed separation points. In order to minimize the total mass of the oscillating components, a small carbon fiber plate was attached to the wing at the root, and a larger stationary aluminum plate was placed 1 mm above the moving plate [see Fig. 3(b)]. The oscillating carbon fiber plate extends  $0.15c$  upstream of the wing leading edge,  $0.15c$  downstream of the trailing edge, and  $\pm 0.8c$  in the cross-stream direction (larger than the leading-edge vortex, which was typically no more than  $0.25c$  in diameter). The fixed end plate extends  $2c$  upstream and  $10c$  downstream, and the full width of the water tunnel in the cross-stream direction. A distance of  $2c$  is maintained between the wing tip and the bottom wall of the water tunnel. The wing is connected to the translation mechanism through a rotation stage, which allows

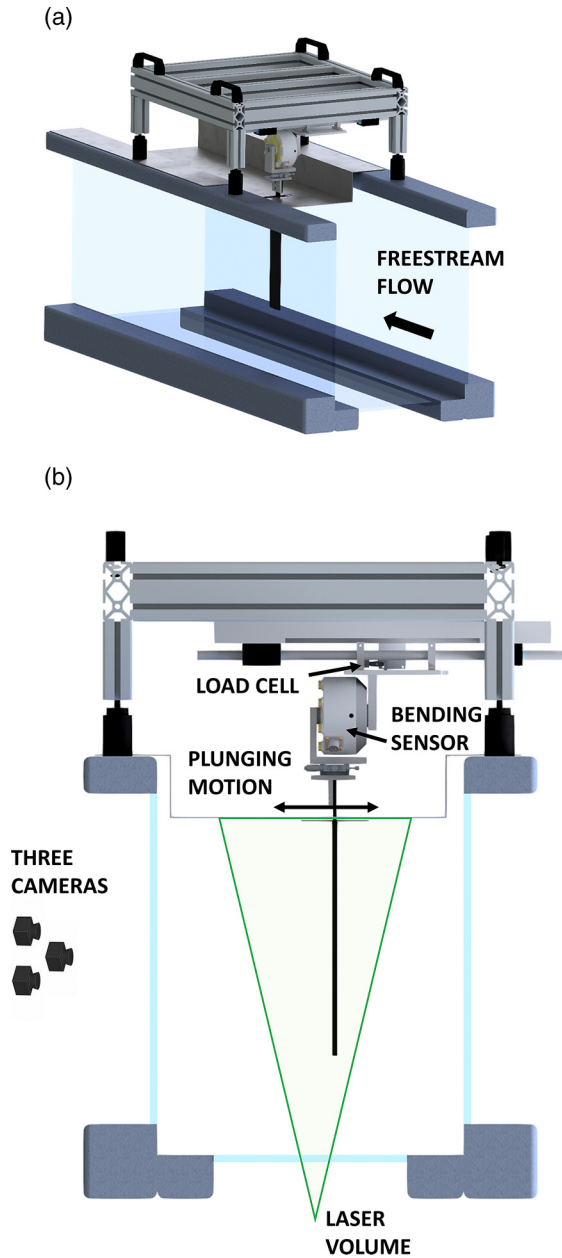


FIG. 3. Test rig: (a) isometric view, (b) front view.

variation of the geometric angle of attack with an accuracy of  $\pm 0.2^\circ$ . The moving carriage is held by four air bearings that absorb the bending and torque loads while enabling frictionless motion. A Zaber LSQ150B-T3 translation stage powered by a stepper motor provides a sinusoidal plunging motion with an accuracy of 2% of peak-to-peak amplitude.



### B. Force and moment measurements

Both unsteady lift force and bending moment were measured. For lift force, an S-beam load cell is placed between the moving platform and the motorized translation stage, i.e., normal to the freestream flow (see Fig. 3). A moment sensor is placed between the wing and moving platform to measure the bending moment, i.e., the moment vector component around the freestream direction ( $x$  axis). For the lift sensor, the Futek JR S-Beam load cell (FSH00103) has a range of  $\pm 22.24$  N. For the moment sensor, the Futek Low Profile Thrust and Moment Load Cell (FSH01954-MTA500) has a range of  $\pm 11.30$  Nm. The moving carriage also includes an accelerometer (Strainsense 4807A) which is used to remove inertia forces due to the moving parts. To remove this component, the structural mass and inertial moment were multiplied by the instantaneous acceleration during the plunging motion. The calculated inertia force and moment are then subtracted from the raw signal to calculate the net aerodynamic loads.

For measurements of stationary wings, the data were acquired for 60 s at an acquisition rate of 1 kHz. For dynamic measurements, the acquisition rate was set to 2000 samples per period and the data were acquired for 55 plunging periods. The first five periods are excluded from the data analysis. From the remaining 50 periods of data, phase-averaged lift and moment are extracted.

Here the lift coefficient  $C_L$  and bending moment coefficient  $C_{M_x}$  are defined as

$$C_L = \frac{L}{0.5\rho U_\infty^2 S}, \quad (3)$$

$$C_{M_x} = \frac{M_x}{0.5\rho U_\infty^2 S b}, \quad (4)$$

where  $L$  is the lift force,  $M_x$  is the bending moment, and  $S$  is the planform area. The uncertainty in the measurement of lift coefficient  $C_L$  is estimated to be  $\pm 0.05$  for static measurements and  $\pm 0.15$  for dynamic measurements. The uncertainty is based on 95% confidence intervals [31,32]. The uncertainty in the measurement of bending moment coefficient  $C_{M_x}$  for the unsteady data is estimated to be  $\pm 0.06$ .

### C. Volumetric velocity measurements

Three-dimensional velocity measurements were acquired on the volume over the suction side of the wing using the TSI volumetric velocimetry system (V3V<sup>TM</sup>) based on the defocusing digital particle image velocimetry (DDPIV) technique [33]. The volume of interest was illuminated with a Nd:YAG 200-mJ pulsed laser. The laser beam was converted into a cone through two cylindrical lenses offset by  $90^\circ$  from each other. The cone was projected towards the wing with a  $45^\circ$  mirror from the wing tip side along the spanwise direction (Fig. 3). The water tunnel was seeded with 50- $\mu$ s hollow glass particles. For a single velocity field acquisition, two laser pulses were fired 800  $\mu$ s apart. The images were acquired using three 4MP 12 bit charge-coupled device cameras placed to form an equilateral triangle whose common focal plane defines the most distant plane within the volume of interest. The camera lenses were AF Nikkor 50 mm f/1.8D. Multiple defocused particle images were generated where separation distance and location give the particle position in three-dimensional space. If the three images of a single particle were superimposed, the particle would appear as a triplet with its center equating to its  $x$ - $y$  coordinates and the size of the triangle equating to its  $z$  coordinate. The cameras were calibrated by translating a rectangular plate of regularly spaced grid dots across the volume of interest with image triplets acquired at 5 mm intervals to generate a mapping between three-dimensional spatial position of a particle and a triplet of local positions on the three cameras. The images acquired by the three cameras are converted into a single gridded three-component velocity field through four main steps: (i) an identification algorithm detects the particles in each of the six images (three per laser pulse); (ii) each particle is matched with its counterpart in the three images of the same laser pulse using the triplets generated during the calibration stage, generating a list of triplets; (iii) an algorithm for 3D particle tracking [34] is



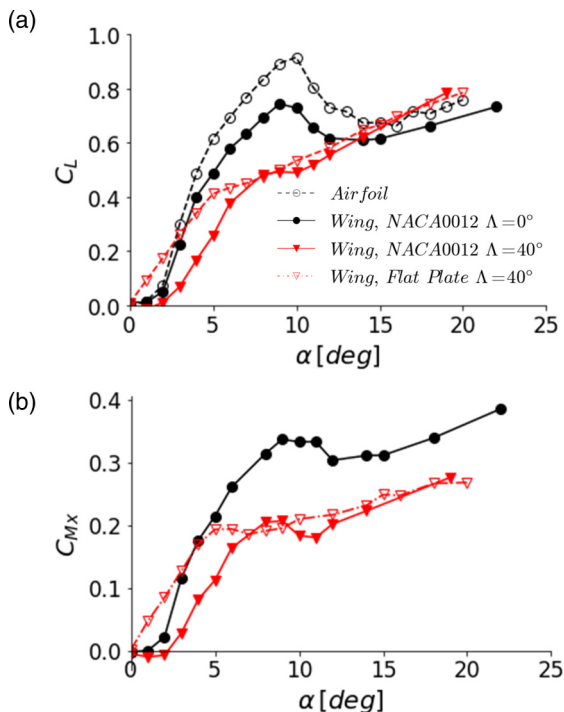


FIG. 4. (a) Lift coefficient, (b) bending moment coefficient of the stationary wings.

used to match each triplet in the two pulses; (iv) this produces randomly spaced velocity vectors, which are then interpolated onto a regular grid. The measurement uncertainty of the instantaneous velocity is estimated to be less than 3% of the freestream velocity.

The phase-averaged flow field is obtained by the acquisition of 100 image pairs for a fixed phase during the plunging motion, timed through an optical linear encoder. A convergence study showed that 100 cycles are sufficient for the phase-averaged quantities. Measurements are taken at phase intervals of  $t/T = 0.125$ , where  $T$  is the plunging period. For each phase, the vectors were interpolated onto a  $140 \times 140 \times 100$ -mm grid with uniform voxel size of 4 mm, and the phase-locked average was calculated over 100 snapshots. In order to cover the full span of the wings (313.5 mm), four separate volumes were acquired along the spanwise direction. These volumes were merged together into a common grid through interpolation. In order to identify the major vortical structures, the velocity vector field was processed to extract the  $Q$ -criterion parameter, which allows an improved distinction between vortical structures and shear flows [35]. Indeed, its definition,  $Q = 0.5(\|\Omega\|_E^2 - \|S\|_E^2)$ , represents the difference of Euclidean norm of vorticity tensors,  $\Omega = 0.5(\nabla u - \nabla u^T)$ , and strain rate,  $S = 0.5(\nabla u + \nabla u^T)$ . Hence,  $Q > 0$  indicates a vortex dominated flow.

### III. RESULTS AND DISCUSSION

Figure 4 shows the variation of the time-averaged lift coefficient  $C_L$  and bending moment coefficient about the root  $C_{Mx}$  as a function of angle of attack for stationary wings. The static aerodynamics is compared for the three wings with the same aspect ratio of  $AR = 10$ : the unswept wing, and the swept wings with a NACA0012 airfoil cross section and flat-plate cross section. For comparison, the lift coefficient of the airfoil (with end plates at both ends) is also given. The lift coefficient of the NACA 0012 airfoil, including its peculiar variation for small angles of attack

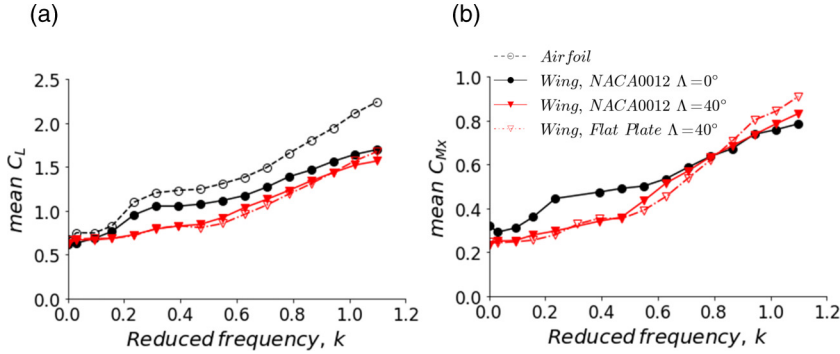


FIG. 5. Variations of the time-averaged (a) lift coefficient, (b) bending moment coefficient with reduced frequency,  $\alpha = 15^\circ$ .

( $\alpha \leq 3^\circ$ ) and the comparison with the literature at this Reynolds number, can be found in Ref. [36]. This peculiar variation, although with smaller gradient, is also observed for the unswept and swept wings with the NACA 0012 airfoil cross section. The wing with the flat-plate cross section does not exhibit this phenomenon, in line with the expectations for 2D flat-plate airfoils reported in the literature. Except in the region of very small angles of attack, the lift of the finite wings is smaller than that of the airfoil due to the effect of the finite span, and for the swept wings, the “independence principle” [37]. The lift and the bending moment variations are qualitatively similar.

We focus on the post-stall angle of attack of  $\alpha = 15^\circ$  for the plunging wing experiments as this regime exhibits large unsteady forces due to the promotion of leading-edge vortex formation. Figure 5 presents the time-averaged lift and bending moment coefficients as a function of reduced frequency  $k$ . The mean lift coefficient generally increases with increasing reduced frequency. Its variation is qualitatively similar to that of the airfoil. However, the effects of the finite span and the sweep angle can be seen as expected. The difference between the two swept wings is negligible, although the gradient of the lift coefficient becomes steeper at high reduced frequencies for the flat-plate wing. Generally, the qualitative variation of the mean bending moment coefficient is similar to that of the lift coefficient. However, when closely studied, significant differences appear with increasing reduced frequency. The gradient of the moment curve is the largest for the swept wing with the flat-plate cross section, followed by that of the swept wing with the NACA0012 airfoil cross section. The bending moment is larger for the swept wings at high reduced frequencies. As there is an indication of changing flow physics at high frequencies, we will focus on the highest reduced frequency tested,  $k = 1.1$ .

Figure 6 presents the phase-averaged lift and bending moment coefficients as a function of effective angle of attack  $\alpha_{\text{eff}}$  [see Eq. (2)] at  $k = 1.1$ . All lift and moment loops have a clockwise direction and the data symbols show the eight phases at which the phase-averaged velocity was obtained. At  $t/T = 0$  when the effective angle of attack is equal to the mean angle of attack, the flow over the wings is mostly attached as will be shown later. Consequently, the lift of the unswept wing is smaller than that of the airfoil as expected (effect of the finite span). The lift of the swept wings is smaller than that of the unswept wing, in line with the “independence principle.” At this instant, the lift of the swept wing with the flat-plate cross section is slightly larger than that of the swept wing with the NACA0012 airfoil cross section. As the wing effective angle of attack increases to a maximum, the lift for all three wings goes through a maximum, and the differences between them vanish. As the wings and the airfoil reach their maximum lift near the maximum effective angle of attack, the added mass contribution estimated from the Theodorsen’s formulation for a flat-plate airfoil becomes zero. Hence, the circulatory forces determine the maximum lift force for the wings, similar to airfoils [36]. The variation of the bending moment between  $t/T = 0$  and  $t/T = 0.25$  is qualitatively similar to that of the lift.

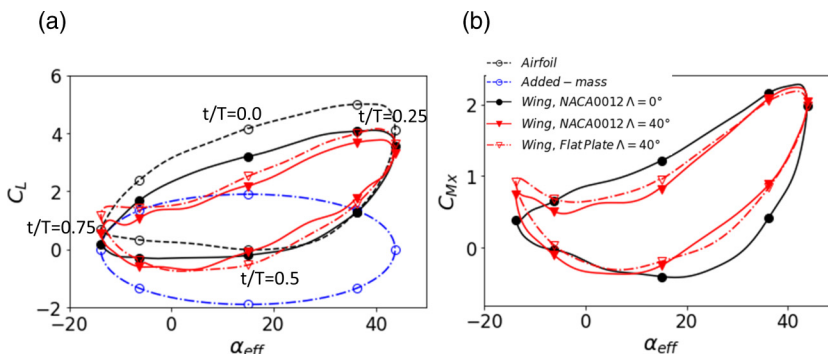


FIG. 6. Variation of the (a) lift coefficient, and (b) bending moment coefficient for  $\alpha = 15^\circ$ ,  $k = 1.1$ ,  $A/c = 0.5$ .

As the effective angle of attack starts to decrease, the differences between the lift of the wings remain small, whereas the bending moment of the unswept wing first shows some departure from the other two before converging again around  $t/T = 0.5$ . As the effective angle of attack reaches a minimum at  $t/T = 0.75$ , large differences between the lift and moment of the three wings appear. Around this phase the shape of the moment loops are distinctly different, exhibiting a cusp, in particular for the swept wings. We will show by means of velocity measurements that this behavior is due to the different nature of the deformation of the leading-edge vortex on the unswept and swept wings.

Top views of the three wings in Fig. 7 reveal the isosurfaces of the  $Q$ -criterion magnitude,  $Qc/U_\infty = 100$ , colored by the magnitude of spanwise velocity  $w_{LE}$  (parallel to the wing leading edge) at  $t/T = 0, 0.125$ , and  $0.250$ . In addition, near-surface streamlines over the suction surface of the wing are shown. The near-surface streamlines are obtained on a surface parallel to the wing surface and at a distance of 2 mm ( $3\%c$ ). As this distance is a small fraction of the chord length, we believe that the streamline patterns are a good approximation to the surface topology. In Fig. 7, the regions between the dashed lines and the root (symmetry plane) have poor data quality because of the laser reflections as well as a limited field of view for the camera trio, and consequently are not shown. The left column shows the unswept wing, the middle column the swept wing with the NACA0012 cross section, and the right column the swept wing with the flat-plate cross section. At the top of the motion  $t/T = 0$ , any vortical flow appears to have left the measurement volume and the flows over the wings are mostly attached. At  $t/T = 0.125$ , as the wing moves downward, the leading-edge vortex starts to develop, but this is only visible for the swept wing with the flat-plate cross section. At  $t/T = 0.250$ , the leading-edge vortices are similar to straight vortex filaments, and parallel to the leading edges. A clear indication of the tip vortex is only visible for the swept wing with the flat plate cross section. For swept wings, streamlines suggest the reattachment of the flow downstream of the vortices. As Fig. 6 reveals that maximum lift occurs near  $t/T = 0.250$ , at the maximum effective angle of attack, it appears that the maximum lift is reached during the formation process of the leading-edge vortices, long before they grow and shed. This is similar to the findings for two-dimensional airfoils [36]. While there is virtually no spanwise flow along the vortex filament for the unswept wing, there is spanwise flow in the vortices over the swept wings towards the wing tip.

The top views in Fig. 8 reveal corresponding vortical flows and near-surface streamlines at  $t/T = 0.375$  and  $0.500$ , as the lift and moment are decreasing (see also Fig. 6). Due to the continuous shedding and roll-up of the vorticity, one observes leading-edge vortices becoming stronger, while remaining mostly parallel to the leading edges of the wings. However, at  $t/T = 0.5$  when the wing is at the bottom of the motion, some three-dimensionality of the vortex filaments becomes noticeable at both ends. Near-surface streamlines and isosurfaces of the  $Q$ -criterion parameter suggest the legs

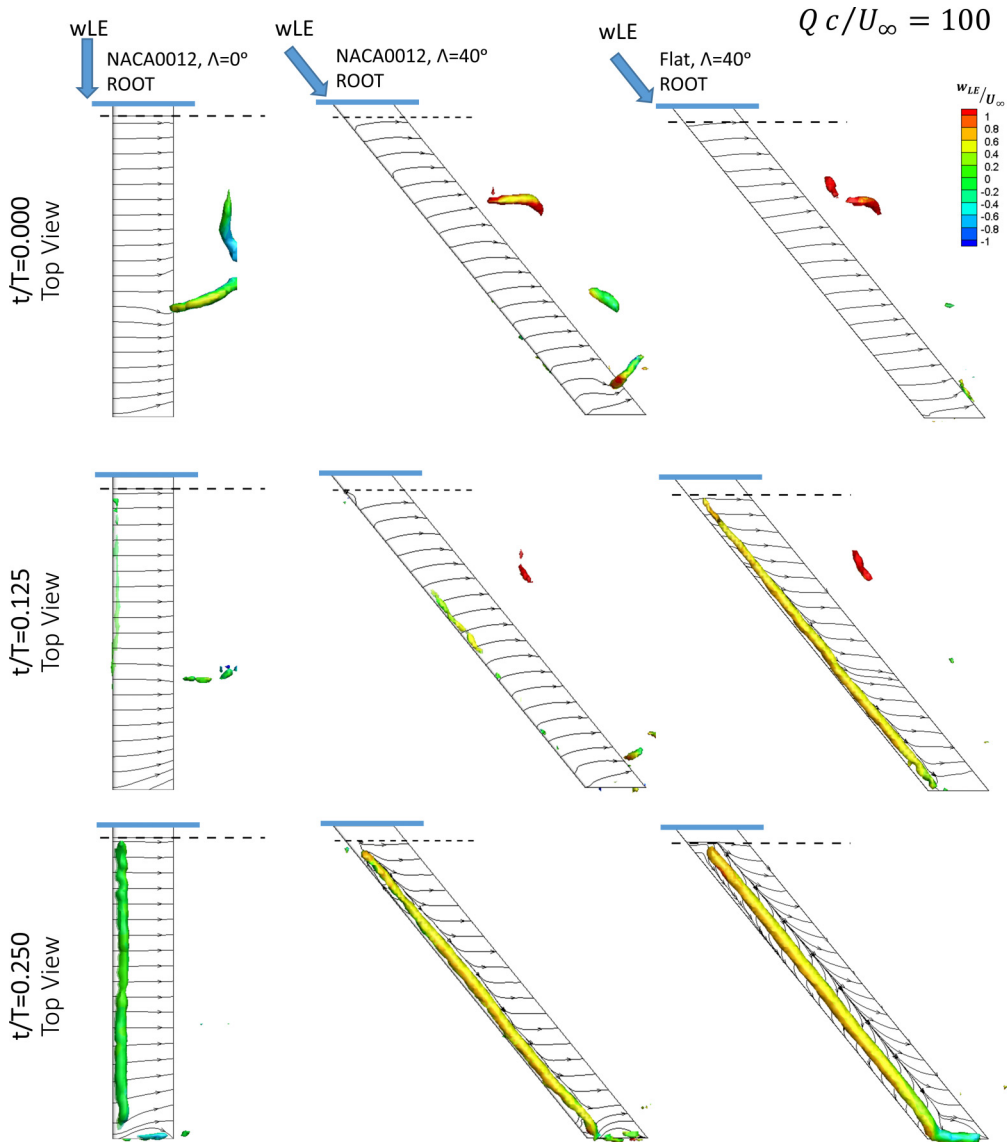


FIG. 7. Iso-surfaces of  $Qc/U_\infty = 100$  and near-surface streamlines,  $\alpha = 15^\circ$ ,  $k = 1.1$ ,  $A/c = 0.5$ . Top views of the unswept wing (left column), swept wing with airfoil cross section (middle column), swept wing with flat-plate cross section (right column);  $t/T = 0$  (top row),  $t/T = 0.125$  (middle row),  $t/T = 0.250$  (bottom row).

of the vortex filament become almost perpendicular to the surface near the wing tip for the unswept wing and near both the wing tip and root for the swept wing with NACA 0012 cross section. There is a region with reversed spanwise flow in the vortex filament near the wing tip for the unswept wing. Side views at the corresponding times reveal a contrasting behavior of the tip vortex for the two swept wings. While the tip vortex and leading-edge vortex remain attached to the wing for the swept wing with the NACA0012 airfoil cross section, the tip vortex appears to shed for the swept wing with the flat-plate cross section. For both wings, the vortex filament initially appears to be attached to the surface near the root, similar to the leading-edge vortices over delta wings.

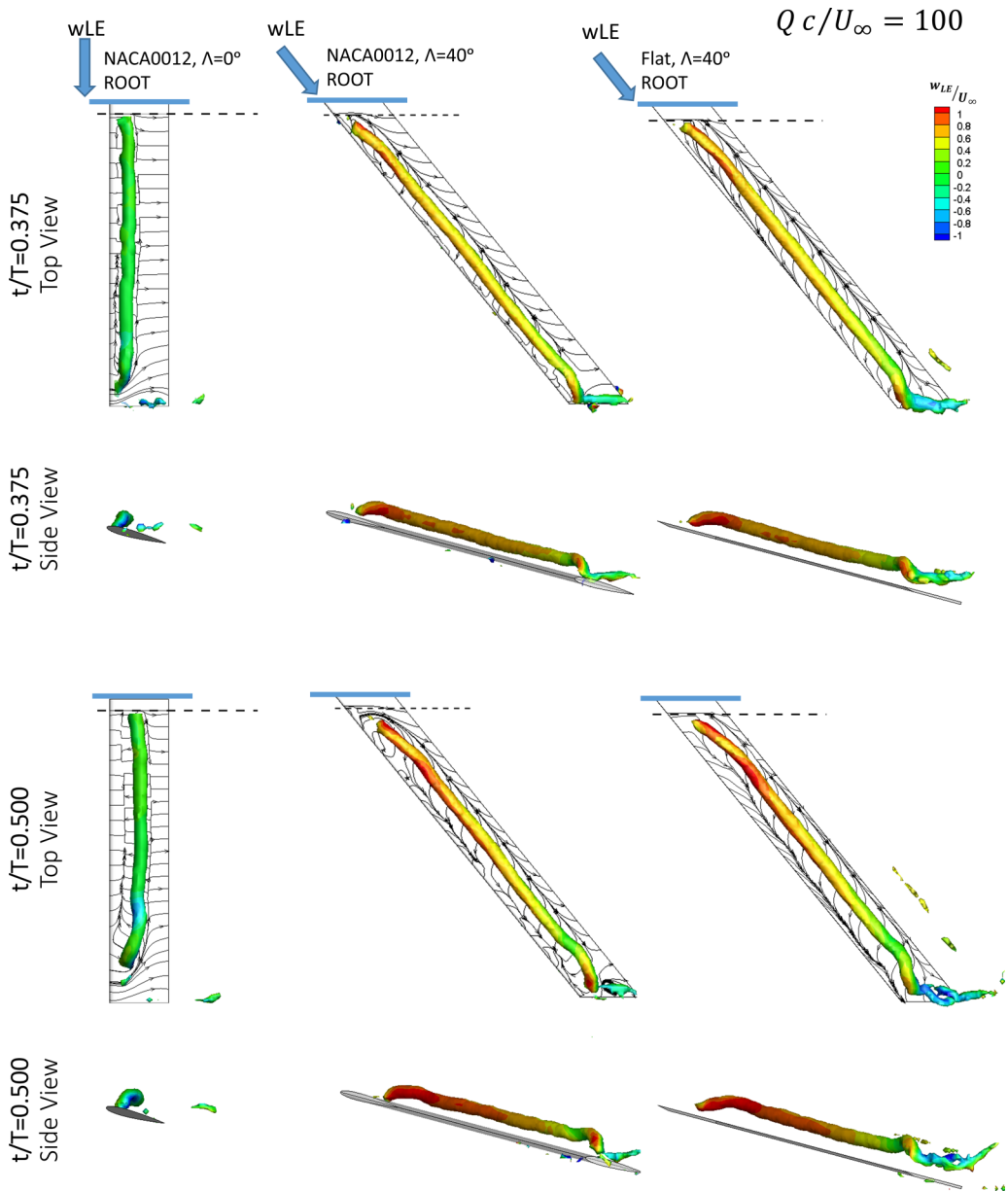


FIG. 8. Isosurfaces of  $Qc/U_\infty = 100$  and near-surface streamlines,  $\alpha = 15^\circ$ ,  $k = 1.1$ ,  $A/c = 0.5$ . Top and side views of the unswept wing (left column), swept wing with airfoil cross section (middle column), swept wing with flat-plate cross section (right column);  $t/T = 0.375$  (top),  $t/T = 0.500$  (bottom).

As the wing begins the upstroke ( $t/T = 0.625$ ) and reaches the minimum effective angle of attack at  $t/T = 0.750$ , the leading-edge vortices nearly approach the trailing edge of the wings (see Fig. 9). The leading-edge vortex appears to remain normal to the root plane for the unswept wing, implying that the boundary condition is similar to that of a symmetry plane. At these two instants, flow separation on the wing surface upstream of the vortices is noticeable. The leading-edge vortex on the unswept wing significantly deforms near the wing-tip end, and is nearly perpendicular to

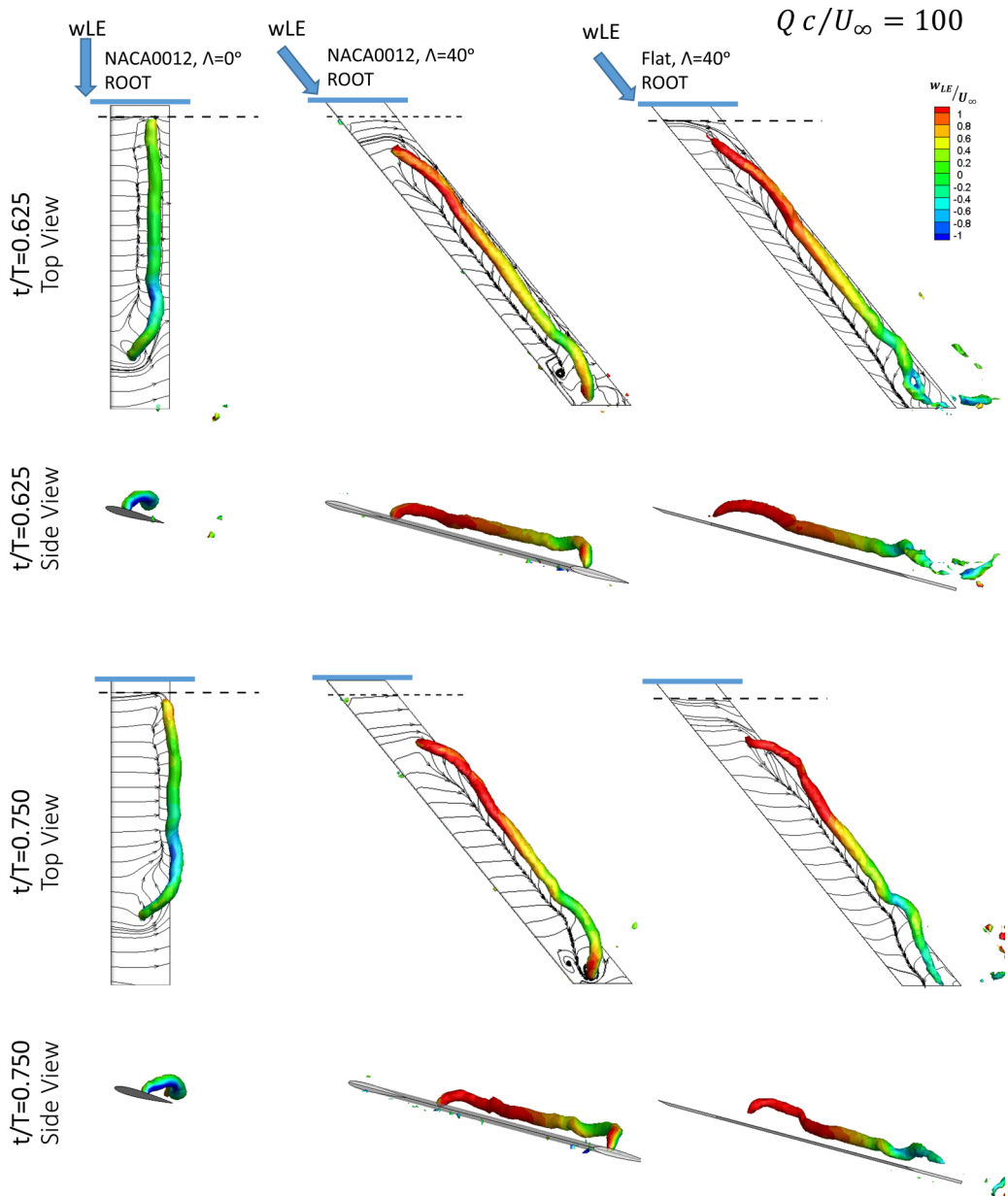


FIG. 9. Isosurfaces of  $Qc/U_\infty = 100$  and near-surface streamlines,  $\alpha = 15^\circ$ ,  $k = 1.1$ ,  $A/c = 0.5$ . Top and side views of the unswept wing (left column), swept wing with airfoil cross section (middle column), swept wing with flat-plate cross section (right column);  $t/T = 0.625$  (top),  $t/T = 0.750$  (bottom).

the surface. This is similar to the observation for a low aspect ratio wing [21]. It is seen in Fig. 9 that the leg is further away from the wing tip. Again, there is a region of reverse spanwise flow in the filament inboard of the leg near the wing tip. The end of the filament near the root appears to be attached (this is also supported by the downstream view shown in Fig. 10). In contrast, the leading-edge vortices over the swept wings extend closer to the wing tip, while the root end of the vortex moves outboard. The side views again confirm that the vortex filament is attached to

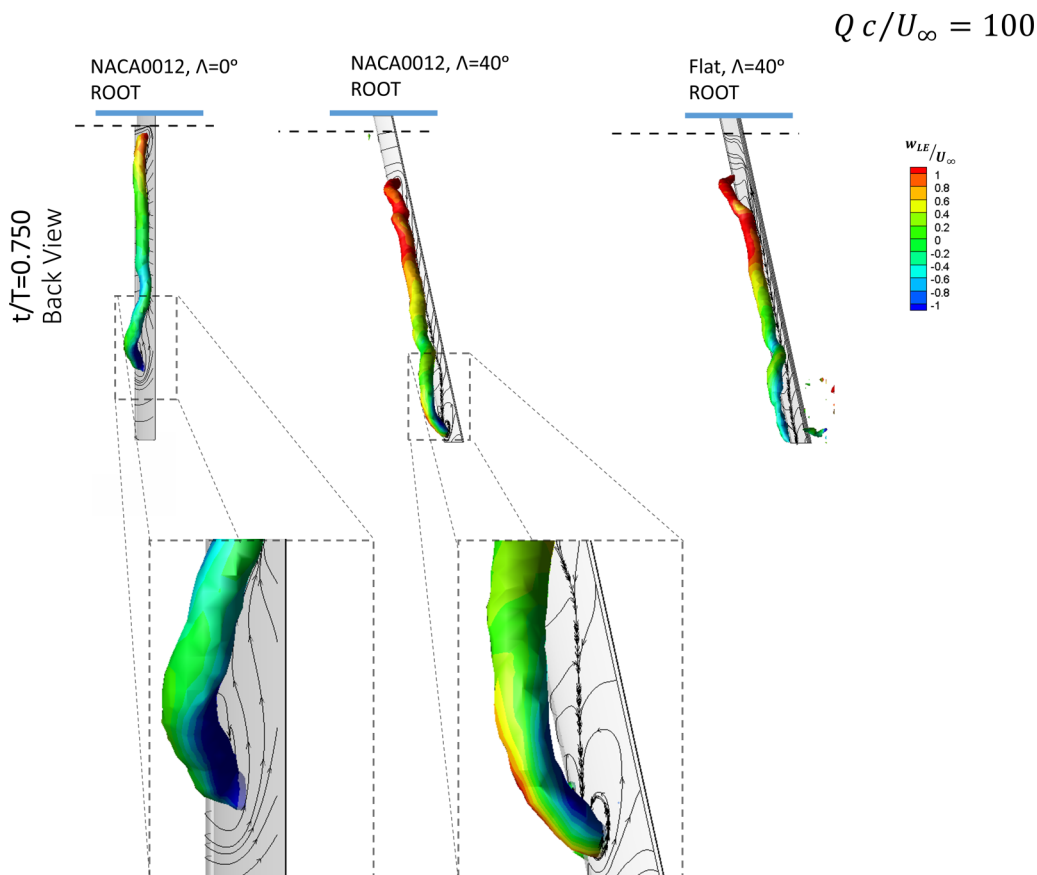


FIG. 10. Iso-surfaces of  $Qc/U_\infty = 100$  and near-surface streamlines,  $\alpha = 15^\circ$ ,  $k = 1.1$ ,  $A/c = 0.5$ . Rear view of the unswept wing (left column), swept wing with airfoil cross section (middle column), swept wing with flat-plate cross section (right column);  $t/T = 0.750$ .

the surface for the swept wing with the NACA0012 airfoil cross section, whereas the leading-edge vortex appears to be further away from the wing surface for the swept wing with the flat-plate cross section. For both swept wings, the leading-edge sheds and moves away from the root plane.

Figure 10 shows the downstream views for the three wings at  $t/T = 0.750$ . For the wings with the NACA0012 airfoil cross section, both legs are attached to the wing surface. However, the wing-tip end of the filament appears to shed for the swept wing with the flat-plate cross section. Figure 10 summarizes the major difference between the swept and unswept wings at this instant. The leg near the wing tip shifts inboard for the unswept wing, and the leg near the root shifts outboard for the swept wings. We recall from Fig. 6 that the swept wings have larger bending moment than the unswept wing at  $t/T = 0.750$ , exhibiting a cusp in the moment loops when the effective angle of attack is minimum. It is well established that leading-edge vortices are associated with low pressure on the upper surface [4], and that where these vortices anchor to the upper surface there is a low pressure region [21]. Hence the larger bending moment observed for the swept wings is consistent with the spanwise position of the leading-edge vortices revealed by the velocity measurements.

When the top and side views in Fig. 9 and downstream views in Fig. 10 are examined together, it becomes clear that spanwise flow (parallel to the leading edge) shows strong dependence on the vortex orientation. This is illustrated in the enlarged views of the filament legs for the unswept wing and the swept wing with the NACA0012 airfoil cross section. The enlarged views in Fig. 10 of



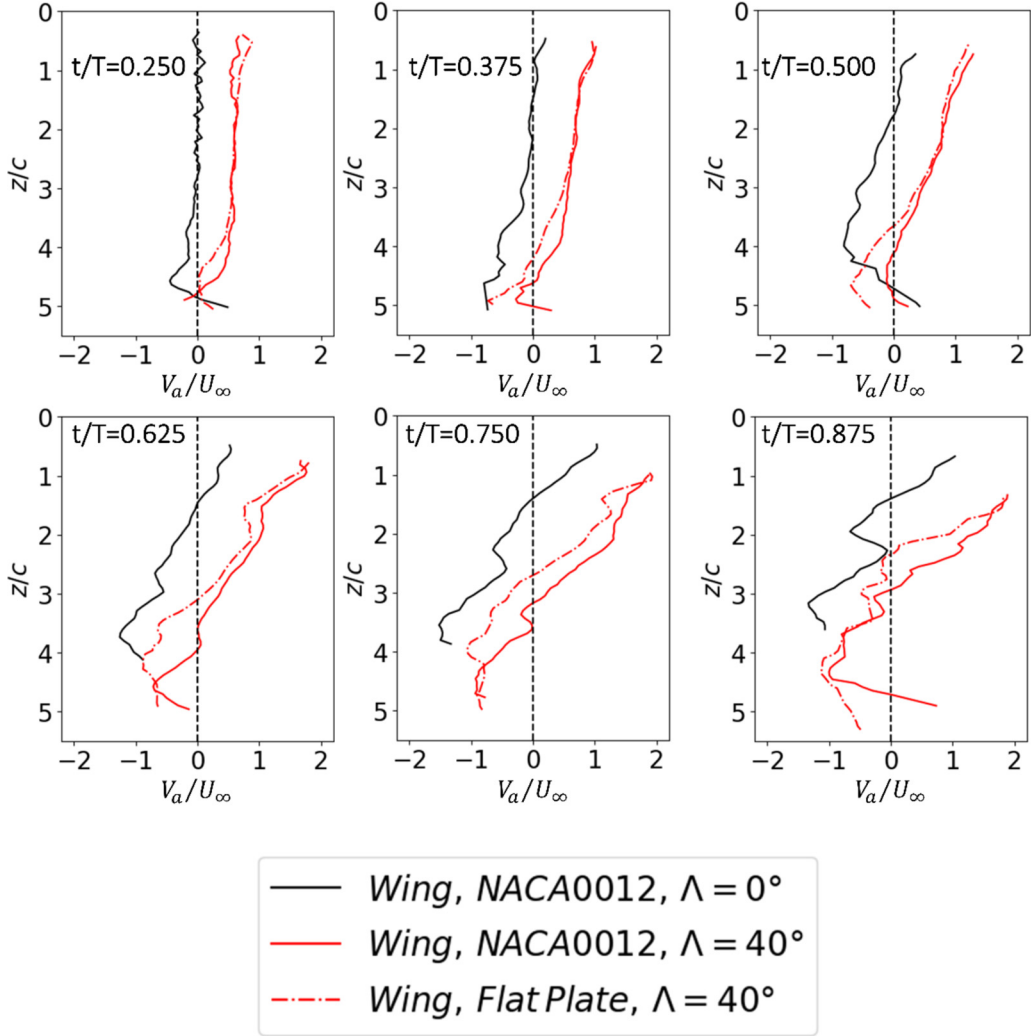


FIG. 11. Variation of the phase-averaged axial velocity at the vortex center,  $\alpha = 15^\circ$ ,  $k = 1.1$ ,  $A/c = 0.5$ .

the filaments near the wing surface show both positive (towards the tip) and negative (towards the root) velocity components parallel to the leading-edge in different parts of the isosurfaces. Both cases reveal a negative velocity component downstream side of the isosurfaces, whereas there is a positive velocity component upstream and above the filament. This is consistent with the swirling of the flow around the vortex filament near the surface. We note that this qualitatively similar to the observations for a plunging low aspect ratio wing [21].

It is noted that the isosurfaces of the  $Q$ -criterion magnitude colored by the velocity component parallel to the leading edge, discussed in previous figures, do not reveal the axial flow structure inside the vortex core near the vortex axis. They simply give an indication of external spanwise flow outside the vortex core. In order to examine the axial flow structure in the vortex core, the vortex center was found by identifying the location of the maximum  $Q$ -criterion parameter at each section along the filament, and then calculating the velocity component along the vortex axis. The variation of the axial velocity  $V_a$  at the vortex center for the three wings at various instants are shown in Fig. 11. The gradient of the axial velocity magnitude at the vortex center increases as the

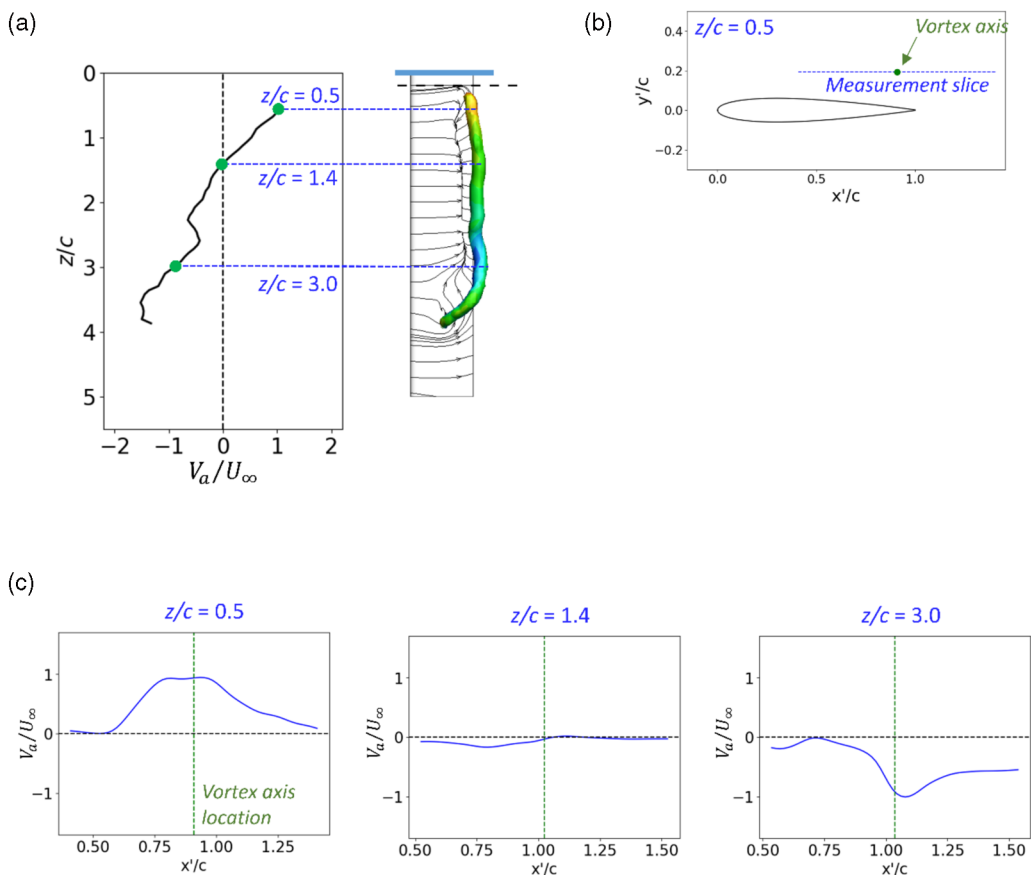


FIG. 12. (a) Axial velocity at the vortex center; (b) example of the measurement line at  $z/c = 0.5$  station; (c) axial velocity profiles along the chordwise coordinate at three stations,  $\Lambda = 0^\circ$ ,  $\alpha = 15^\circ$ ,  $k = 1.1$ ,  $A/c = 0.5$ .

effective angle of attack of the wings decreases from a maximum at  $t/T = 0.250$  to a minimum at  $t/T = 0.750$ . At the maximum effective angle of attack, there is virtually no axial flow for the unswept wing, whereas there is some axial flow towards the tip for the swept wings. With decreasing effective angle of attack, axial velocity at the vortex center starts to decrease (become more negative) near the wing tip and the location of zero velocity at the vortex center moves inboard within the filament. The change from positive to negative velocity does not appear to be abrupt. Surprisingly, the magnitude of the reversed axial velocity at the vortex center is the largest for the unswept wing. This is thought to be associated with the largest deformation of the vortex filament as documented in the previous figures. Generally, the axial velocity magnitude is similar for the two swept wings. The magnitude of the negative (reversed) axial velocity is somewhat larger for the unswept wing with the flat-plate cross section.

We also studied the variation of the axial velocity within the core for  $t/T = 0.750$  when the gradient of the axial flow variation is the largest. Figure 12 shows the axial velocity profiles as a function of chordwise distance at three stations for the unswept wing. Jetlike (at  $z/c = 0.5$ ), nearly uniform (at  $z/c = 1.4$ ), and wakelike (at  $z/c = 3.0$ ) axial velocity profiles are observed. The profile at  $z/c = 3.0$  reveals the nonaxisymmetric nature of the vortex and the external flow. Figure 13 shows the axial velocity profiles at five stations for the swept wing with the NACA0012 airfoil cross section at the same instant. Again jetlike (at  $z/c = 1.1$ ), nearly uniform (at  $z/c = 2.8$ ), and wakelike

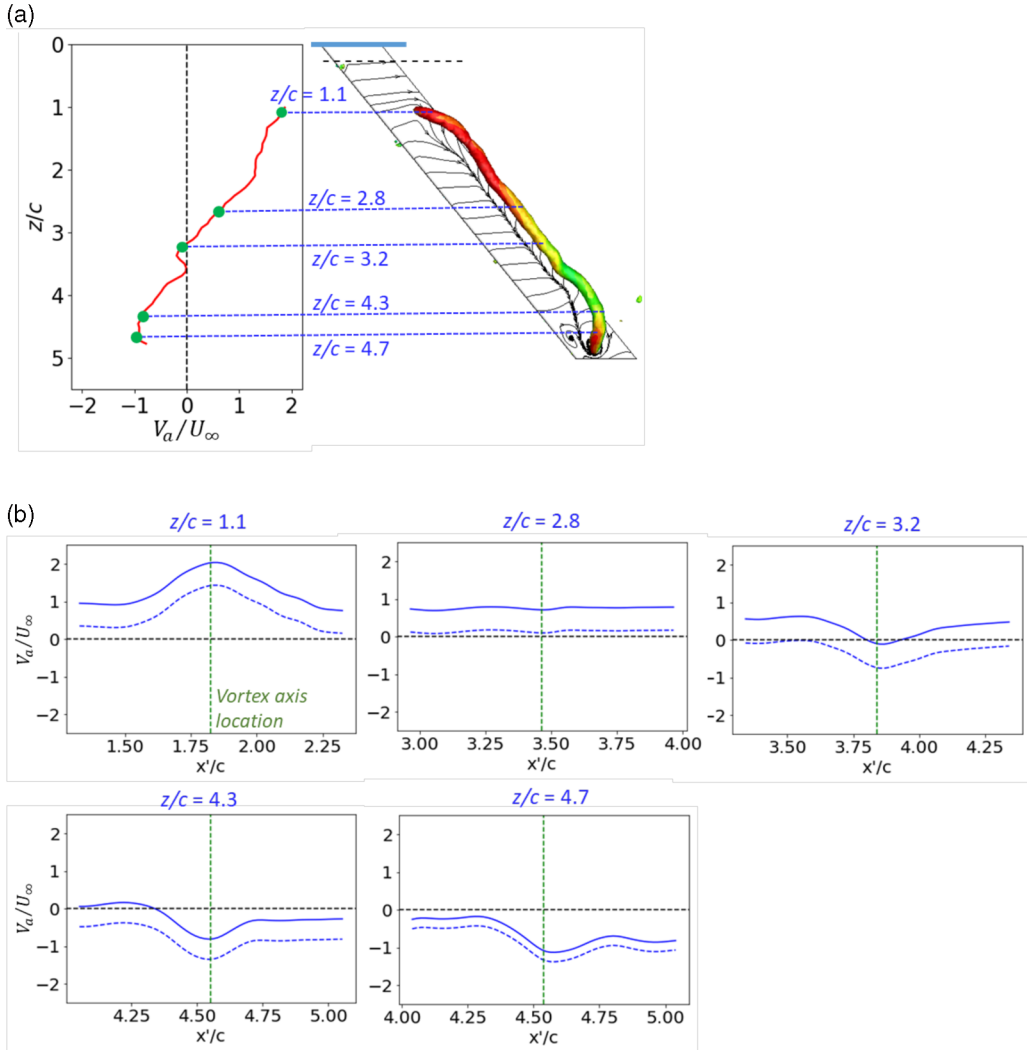


FIG. 13. (a) Axial velocity at the vortex center; (b) axial velocity profiles (solid lines) and with spanwise component of freestream removed (dashed lines) along the chordwise coordinate at five stations,  $\Lambda = 40^\circ$ ,  $\alpha = 15^\circ$ ,  $k = 1.1$ ,  $A/c = 0.5$ .

(at  $z/c = 3.2, 4.3, 4.7$ ) axial velocity profiles are found. Once the reversed flow is established, the vortex and the external flow cease to be axisymmetric. The last two stations are in the region where the vortex filament changes its orientation from being nearly parallel to the leading edge to being nearly perpendicular to the wing surface. Nonaxisymmetric axial velocity profiles at these two stations are related to the deformation of the vortex filament.

The axial velocity shown in Figs. 11–13 reveals that its magnitude can reach twice the freestream velocity. This is much greater than the spanwise flow component of the freestream velocity ( $0.64U_\infty$  in magnitude). In order to make this more explicit, we subtracted this component from the velocity vector field and the resulting axial velocity magnitude is added to Fig. 13(b) with dashed lines. It is seen that high axial velocities in the vortex core cannot be explained by the spanwise component of the freestream velocity. The jetlike and wakelike axial velocity profiles still exist even if this component of the freestream velocity is removed. It is typical to observe jetlike axial velocities

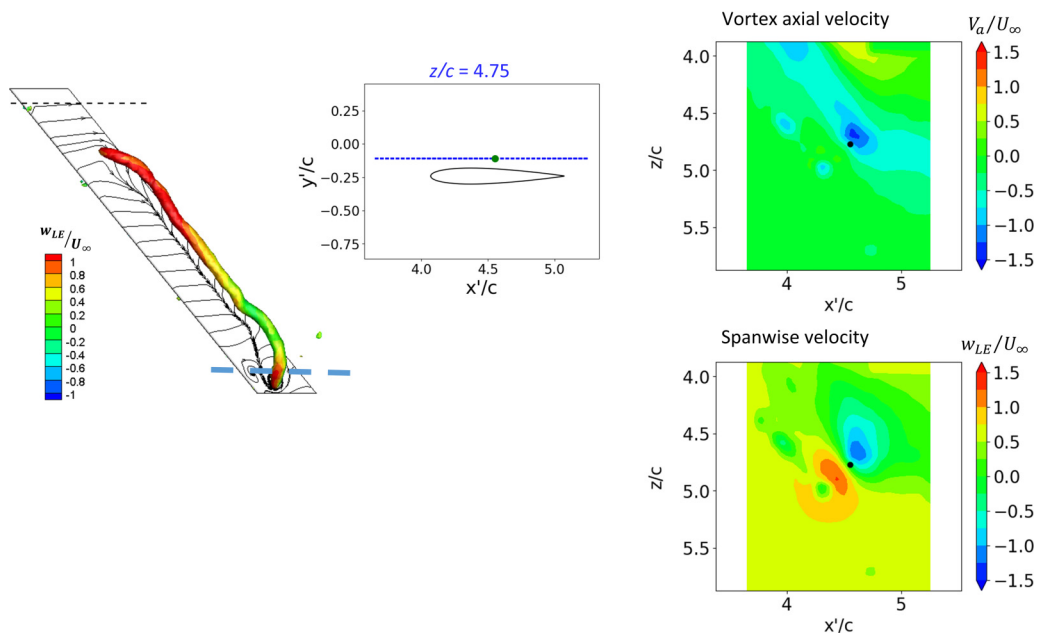


FIG. 14. Contour plots of axial velocity and spanwise velocity in the plane shown,  $\Lambda = 40^\circ$ ,  $\alpha = 15^\circ$ ,  $k = 1.1$ ,  $A/c = 0.5$ .

larger than the freestream velocity on delta wings with comparable sweep angles [38]. The jetlike and wakelike axial velocity profiles observed in our experiments and the gradual transition between the two have some similarities with those observed on nonslender delta wings ( $\Lambda \leq 55^\circ$ ) as discussed previously [39]. For nonslender delta wings, maximum jetlike velocities are not as high as those observed on slender delta wings ( $\Lambda \geq 65^\circ$ ), and vortex breakdown is much less abrupt compared to breakdown over slender delta wings.

Figure 14 shows the contour plot of the axial velocity  $V_a$  in a plane that contains the last station ( $z/c = 4.75$ ) discussed above and that is parallel to the wing chord line. The black dot shows the location of the vortex center. Although there is nonaxisymmetry, strong negative velocity illustrates the upward motion of the fluid in the core. Also shown is the contour plot of the spanwise velocity component  $w_{LE}$  in the same plane. The nonaxisymmetric nature of the surrounding flow is apparent. Both positive and negative velocity regions characterize the swirling flow region around the leg of the vortex filament.

Finally, it is noted that we have observed an indication of a spanwise instability as the leading-edge vortex leaves the trailing-edge region and moves into the wake. This is only apparent for the swept wing with the flat-plate cross section at  $t/T = 0.875$  as shown in Fig. 15. The wavelength of the instability is approximately one chord length ( $\lambda_z/c \approx 1$ ). With the leading-edge flow separation in the post-stall regime at  $\alpha = 15^\circ$  for this Reynolds number, the baseline flow is essentially a mixing layer (at least up to the trailing-edge region). However, this is an oscillating mixing layer (with an oscillating origin). It is well known that spanwise instabilities develop in stationary mixing layers [40]. For the unforced mixing layer, the wavelength in the spanwise direction, normalized by the wavelength in the streamwise direction, was found as  $\lambda_z/\lambda_x = 0.67$  for the naturally developing instabilities. For the forced plunging oscillations of the low aspect ratio wings [19], we estimate a spanwise wavelength around  $\lambda_z/c \approx 1$ , which also corresponds to  $\lambda_z/\lambda_x \approx 1$ . This was most visible in a range of reduced frequencies and for low aspect ratio wings in previous experiments. Here we present evidence of the spanwise instabilities over a plunging high aspect ratio swept wing. We suggest that there could well be common flow physics with the naturally developing mixing layers.

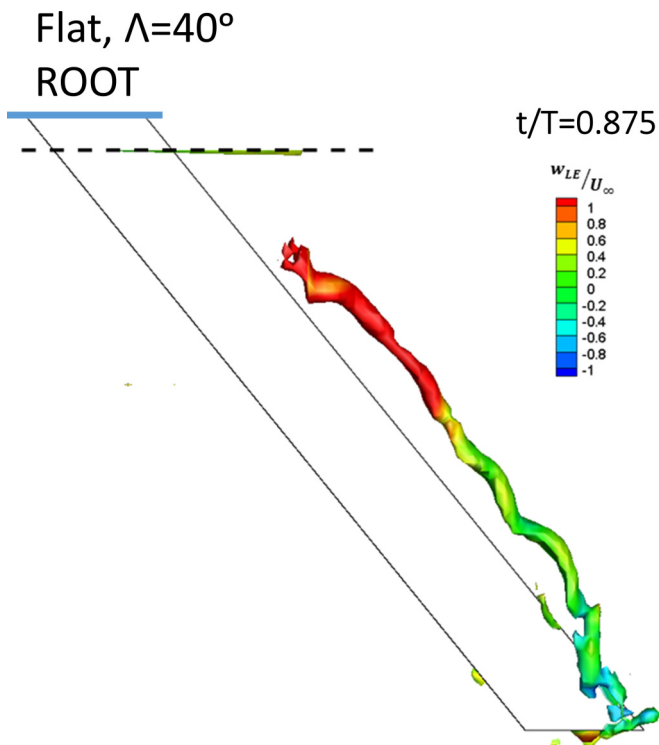


FIG. 15. Isosurfaces of normalized vorticity magnitude  $\omega c/U_\infty = 13.4$  for  $\alpha = 15^\circ$ ,  $k = 1.1$ ,  $A/c = 0.5$ . Top view of the swept wing with flat-plate cross section;  $t/T = 0.875$ .

It is noted that, in this case, the base flow is a time-varying (periodic) shear flow. However, it is not clear whether the appropriate model is an oscillating mixing layer (a mixing layer with oscillating origin), an oscillating wake, or a vortex filament in order to explain the experimental observation. A recent theoretical work [41] carried out three-dimensional Floquet stability analysis of the *propulsive wake* (hence, resulting in a time-averaged jet) of a plunging airfoil set at a zero mean angle of attack at a low Reynolds number of  $Re = 1700$ . Depending on the Strouhal number and the plunge amplitude, both long wavelength (on the order of  $\lambda_z/c \approx 1$ ) and short wavelength (on the order of  $\lambda_z/c \approx 0.2$ ) instabilities were found to be unstable. However, the mean base flow is essentially a jet flow rather than a mixing layer in their case. Spanwise instabilities in the wake of stationary circular cylinders are well known [42]. Further experimental, computational, and theoretical research on the development of spanwise instabilities of the leading-edge vortices over periodically oscillating wings and the effects of the main parameters (mean angle of attack, sweep angle, amplitude and Strouhal number) is needed.

#### IV. CONCLUSIONS

It is well known that the leading-edge vortices that shed from low aspect ratio wings during unsteady motion exhibit significant deformation and three-dimensionality due to the existence of the wing tip. For high aspect ratio wings, any three-dimensionality of the leading-edge vortex in unsteady wing motion may be more important for the bending moment due to the larger moment arm. We present force, bending moment, and volumetric velocity measurements for aspect ratio  $AR = 10$  plunging wings with sweep angles of  $0^\circ$  and  $40^\circ$ .

The effect of the sweep angle becomes more important on the bending moment than the lift with increasing frequency. It is shown that the bending moment coefficients for both the swept and unswept wings strongly depend on the deformation of the leading-edge vortex filament. The bending moment exhibits the largest departure from that of the quasi-two-dimensional case when the effective angle of attack is minimum.

As the effective angle of attack increases to its maximum, the leading-edge vortex continues to develop mostly parallel to the leading edge. When the wing is at the bottom of the plunging motion, the leg of the leading-edge vortex starts to move inboard on the unswept wing. At the minimum effective angle of attack, the leg of the leading-edge vortex is located near the midchord and inboard of the wing tip, whereas the rest of the vortex is above the trailing edge. In contrast, for the swept wing, the outer leg is still near the wing tip while the leg near the root starts to move outboard, which explains why the bending moment is larger than that of the unswept wing at this instant. The legs of the vortex filament may be attached to the wing or shed, depending on the sweep angle and the wing cross section. These parameters also affected whether the wing tip vortex was attached or shed.

For both sweep angles, there is significant spanwise flow, including towards and away from the wing tip, where the leg touches on the wing. The axial velocity along the vortex filament, which may be towards the wing tip or the wing root (reversed flow), exhibits increasing magnitude as the effective angle of attack decreases and the vortex filament deforms. Axial flow along the vortex filament has the largest magnitudes for the unswept wing. In the vortex core, jetlike, wakelike, and uniform axial velocity profiles were observed. Unlike the classical vortex breakdown, the transition from the jetlike to the wakelike axial flow does not appear to be abrupt. The phase-averaged measurements also revealed evidence of spanwise instabilities in the leading-edge vortex filament for the swept wing with the flat-plate cross section. The wavelength of the spanwise instabilities was on the order of the chord length. It would be interesting to investigate the deformation and instabilities of the vortex filament on flexible oscillating high aspect ratio wings in future research.

#### ACKNOWLEDGMENT

The authors acknowledge the Engineering and Physical Sciences Research Council (EPSRC) (Grants No. EP/M022307/1 and No. EP/S028994/1).

- 
- [1] T. J. Mueller and J. D. DeLaurier, Aerodynamics of small vehicles, *Annu. Rev. Fluid Mech.* **35**, 89 (2003).
  - [2] W. Shyy, H. Aono, S. K. Chimakurthi, P. Trizila, C. K. Kang, C. E.S. Cesnik, and H. Liu, Recent progress in flapping wing aerodynamics and aeroelasticity. *Prog. Aerosp. Sci.* **46**, 284 (2010).
  - [3] M. F. Platzer, K. D. Jones, J. Young, and J. C. S. Lai, Flapping-wing aerodynamics: progress and challenges, *AIAA J.* **46**, 2136 (2008).
  - [4] W. J. McCroskey, Unsteady airfoils, *Annu. Rev. Fluid Mech.* **14**, 285 (1982).
  - [5] Th. von Karman and W. R. Sears, Airfoil theory for non-uniform motion, *J. Aeronaut. Sci.* **5**, 379 (1938).
  - [6] J. Ekaterinaris and M. Platzer, Computational prediction of airfoil dynamic stall, *Prog. Aerosp. Sci.* **33**, 759 (1998).
  - [7] S. Benton and M. Visbal, The onset of dynamic stall at a high, transitional Reynolds number, *J. Fluid Mech.* **861**, 860 (2019).
  - [8] D. E. Rival, J. Kriegerseis, P. Schaub, A. Widmann, and C. Tropea, Characteristic length scales for vortex detachment on plunging profiles with varying leading-edge geometry, *Exp. Fluids* **55**, 1660 (2014).
  - [9] A. Widmann and C. Tropea, Parameters influencing vortex growth and detachment on unsteady aerodynamic profiles, *J. Fluid Mech.* **773**, 432 (2015).
  - [10] K. Ramesh, A. Gopalarathnam, K. Granlund, M. V. Ol, and J. R. Edwards, Discrete-vortex method with novel shedding criterion for unsteady aerofoil flows with intermittent leading-edge vortex shedding, *J. Fluid Mech.* **751**, 500 (2014).

- [11] A. J. Buchner, N. Buchmann, K. Kilany, C. Atkinson, and J. Soria, Stereoscopic and tomographic PIV of a pitching plate, *Exp. Fluids* **52**, 299 (2012).
- [12] A. E. Panah, J. M. Akkala, and J. H. J. Buchholz, Vorticity transport and the leading-edge vortex of a plunging airfoil, *Exp. Fluids* **56**, 160 (2015).
- [13] S. Schreck and H. Helin, Unsteady vortex dynamics and surface pressure topologies on a finite wing, *J. Aircr.* **31**, 899 (1994).
- [14] T. O. Yilmaz and D. Rockwell, Flow structure on finite-span wings due to pitch-up motion, *J. Fluid Mech.* **691**, 518 (2012).
- [15] A. Spentzos, G. Barakos, K. Badcock, B. Richards, P. Wernert, S. Schreck, and M. Raffel, Investigation of three-dimensional dynamic stall using computational fluid dynamics, *AIAA J.* **43**, 1023 (2005).
- [16] A. Spentzos, G. Barakos, K. Badcock, B. Richards, F. Coton, R. A. Galbraith, E. Berton, and D. Favier, Computational fluid dynamics study of three-dimensional dynamic stall of various planform shapes, *J. Aircr.* **44**, 1118 (2007).
- [17] M. Visbal and D. Garmann, Dynamic stall of a finite-aspect-ratio wing, *AIAA J.* **57**, 962 (2019).
- [18] D. Kim and M. Gharib, Experimental study of three-dimensional vortex structures in translating and rotating plates, *Exp. Fluids* **49**, 329 (2010).
- [19] D. Calderon, Z. Wang, I. Gursul, and M. Visbal, Volumetric measurements and simulations of the vortex structures generated by low aspect ratio plunging wings, *Phys. Fluids* **25**, 067102 (2013).
- [20] D. Calderon, Z. Wang, and I. Gursul, Lift-enhancing vortex flows generated by plunging rectangular wings with small amplitude, *AIAA J.* **51**, 2953 (2013).
- [21] M. Visbal, T. O. Yilmaz, and D. Rockwell, Three-dimensional vortex formation on a heaving low-aspect ratio wing: computations and experiments, *J. Fluids Struct.* **38**, 58 (2013).
- [22] A. Gardner, C. Klein, W. Sachs, U. Henne, H. Mai, and K. Richter, Investigation of three-dimensional dynamic stall on an airfoil using fast-response pressure-sensitive paint, *Exp. Fluids* **55**, 1807 (2014).
- [23] K. Kaufmann, C. Merz, and A. Gardner, Dynamic stall simulations on a pitching finite wing, *J. Aircr.* **54**, 1303 (2017).
- [24] N. Chieregin, D. Cleaver, and I. Gursul, Unsteady force and flow measurements for plunging finite wings, Paper 2017-3127, in *47th AIAA Fluid Dynamics Conference, 5-9 June 2017, Denver, Colorado* (AIAA, Reston, VA, 2017).
- [25] I. Gursul and D. Cleaver, Plunging oscillations of airfoils and wings: progress, opportunities, and challenges, *AIAA J.* **57**, 3648 (2019).
- [26] H. R. Beem, D. E. Rival, and M. S. Triantafyllou, On the stabilization of leading-edge vortices with spanwise flow, *Exp. Fluids* **52**, 511 (2011).
- [27] M. R. Visbal and D. J. Garmann, Effect of sweep on dynamic stall of a pitching finite-aspect-ratio wing, *AIAA J.* **57**, 3274 (2019).
- [28] M. Rockwood, A. Medina, D. J. Garmann, and M. R. Visbal, Dynamic stall of a swept finite wing for a range of reduced frequencies, Paper 2019-3335, in *AIAA Aviation 2019 Forum 17-21 June 2019, Dallas, Texas* (AIAA, Reston, VA, 2019).
- [29] K. Onoue and K. S. Breuer, A scaling for vortex formation on swept and unswept pitching wings, *J. Fluid Mech.* **832**, 697 (2017).
- [30] S. Heathcote, Flexible flapping airfoil propulsion at low Reynolds numbers, Ph.D. Dissertation, Department of Mechanical Engineering, University of Bath, Bath, England, UK, 2006.
- [31] R. J. Moffat, Contributions to the theory of single-sample uncertainty analysis, *J. Fluids Eng. - Trans. ASME* **104**, 250 (1982).
- [32] R. J. Moffat, Using uncertainty analysis in the planning of an experiment, *J. Fluids Eng. - Trans. ASME* **107**, 173 (1985).
- [33] F. Pereira and M. Gharib, Defocusing digital particle image velocimetry and the three-dimensional characterization of two-phase flows, *Meas. Sci. Technol.* **13**, 683 (2002).
- [34] S. J. Baek and S. J. Lee, A new two-frame particle tracking algorithm using match probability, *Exp. Fluids* **22**, 23 (1996).
- [35] J. Jeong and F. Hussain, On the identification of a vortex, *J. Fluid Mech.* **285**, 69 (1995).



- [36] N. Chierighin, D. J. Cleaver, and I. Gursul, Unsteady lift and moment of a periodically plunging airfoil, [AIAA J. \*\*57\*\*, 208, \(2019\)](#).
- [37] A. M. Kuethe and C.-Y. Chow, *Foundations of Aerodynamics*, 5th ed. (John Wiley & Sons, New York, 1998), p. 337.
- [38] G. S. Taylor and I. Gursul, Buffeting flows over a low-sweep delta wing, [AIAA J. \*\*42\*\*, 1737 \(2004\)](#).
- [39] I. Gursul, R. Gordnier, and M. Visbal, Unsteady aerodynamics of nonslender delta wings, [Prog. Aerosp. Sci. \*\*41\*\*, 515 \(2005\)](#).
- [40] L. P. Bernal and A. Roshko, Streamwise vortex structure in plane mixing layers, [J. Fluid Mech. \*\*170\*\*, 499 \(1986\)](#).
- [41] L. Sun, J. Deng, and X. Shao, Three-dimensional instabilities for the flow around a heaving foil, [Phys. Rev. E \*\*97\*\*, 013110 \(2018\)](#).
- [42] C. H. K. Williamson, Three-dimensional wake transition, [J. Fluid Mech. \*\*328\*\*, 345 \(1996\)](#).